UNIVERSITY OF GOTHENBURG

Master of Science Thesis

Simulation of attenuation effects in bone scintigraphy

Kaveh Shahgeldi

SUPERVISORS

Peter Bernhardt, Department of Radiation Physics,
University of Gothenburg
And
Michael Ljungberg, Department of Medical Radiation Physics,
Clinical Sciences - Lund, Lund University

DEPARTMENT OF RADIATION PHYSICS
UNIVERSITY OF GOTHENBURG
2009

Abstract

In nuclear medicine, bone scintigraphy is an effective way to diagnose bone metastases. The bone scan index (BSI) method is a quantitative method for estimations of the amount of bone metastases from nuclear images. But BSI is very time consuming and demands several internal and external observers. The software EXINI has been developed to automatically quantify the BSI as well as identify the probability of metastases. However, attenuation effects might have important influence on BSI. The aim of this study was to analyze the attenuation effect in bone scintigraphy.
With help of the Monte Carlo based gamma camera simulation program SIMIND and an NCAT phantom 2D bone scintigraphy images was created. Posterior and anterior net counts were quantified in small tumors; for study of attenuation effects and it's dependents on the tumor´s distance to the camera.

Table of Contents

1. Introduction 4
2. Method & Materials 6
   a. The Monte Carlo Method 6
   b. The NCAT Phantom 7
   c. The Monte Carlo program SIMIND 7
   d. Tumor Locations in NCAT patients 7
   e. The Procedure for Tumor Definitions 9
   f. Scintillation Camera Monte Carlo Simulations 13
   g. Scaling of Simulated SIMIND Images 13
   h. Analysis and Data Processing 13
3. Results 17
4. Discussion 23
5. Conclusion 24
6. Acknowledgements 24
7. References 25

Appendix 1 26

Appendix 2 27

Appendix 3 28

1. Introduction

The most common cancers are breast cancer for women and prostate cancer for men, both metastasize to the bone. Bone scintigraphy can detect bone metastases and is one of the most common nuclear medicine examination methods. It accounts for 25% of nuclear medicine investigations in Sweden and is more sensitive than CT and MRI. Up to 80% of the patients will die from bone metastases as a result of vascular spread and systemic dissemination. Skeleton metastases can be detected with bone scintigraphy; which is an effective way to detect distant tumor spread, as well as it is a more sensitive method than radiographic methods[1]. The radiopharmaceutical used in bone scintigraphy is mainly ^{99m}Tc labeled biphosphonates, ^{99m}Tc-MDP. Infiltration of tumor cells into the skeleton will activate bone cells as osteoblasts, which in its metabolism require phosphor. Therefore, injection of ^{99m}Tc -MDP will revile hotspots areas in the bone scintigram. Whole-body bone scintigraphy can be achieved with continuous imaging obtained in both anterior and posterior projections. Indications for bone scintigraphy are[2]:

- Investigation of suspected or confirmed metastasis in skeleton.
- Staging of tumors, for example in cancer mammae and cancer prostatae.
- Investigation of inflammatory and infectious condition.
- Severe diagnosed fractures, for example, scaphoideum, stress fractures etc.
- Post-treatment of inflammations and tumors

In bone scintigraphy the normal procedure is to measure whole body images in both anterior and posterior view at the same time. Depending on the tumor location the tumors can often be detected more easily from one of the views. However, exactly how this delectability varies with tumor location and interpretation view, i.e. anterior or posterior image, has not been addressed in this work.

It is not always sufficient to simply detect tumors by visual interpretation of the acquired scintigrams. One would like to also have a quantitative estimate of the tumor burden and the involvement of tumor tissues in the skeletal. The calculation of the Bone Scan Index (BSI) is a method for quantitative bone scan interpretation that can be applied for example in advanced prostate cancer. The BSI estimates the fraction of the whole skeleton that is involved by tumor tissue, as well as the regional distribution of the metastases in different bone. BSI is thus an interpretation method for quantifying the amount of total skeleton that is involved by bone metastatic disease. The description of the whole skeleton in a BSI calculation is based on the ICRP publication No.23[3]. In this work an analysis of one hundred fifty-eight individual bones in the body have been performed and expressed as fraction of the weight of the entire skeleton. The BSI is calculated then by summing the product of the weight and the fractional involvement of each bone expressed as percentages of the entire skeleton:

$$BSI = \sum \frac{Spec.Bone}{Entire.skeleton} \times \frac{Tumor}{Spec.Bone} = \frac{Tumor}{Entire.Skeleton}$$

The EXINI Diagnostics Company was founded in Lund 1999, Sweden, by Professor Lars Edenbrandt, and has specialized in Computer–Aided Diagnosis method (CAD) based on nuclear medicine image analysis. With this software it is possible to examine images of heart, brain and whole body bone images acquired with a scintillation camera[4] and from neural network analysis provide some guidance about the severity and outcome of the disease. A recent development have been in bone scan interpretation, where advanced algorithms for segmentation, hot-spot detection and feature extraction make the ground for a quantitative analysis of bone scans and a calculation of the BSI. A diagram illustrating the different steps of the quantification procedure included in EXINI is presented in Figure 1. The software interprets the results and presents a diagnosis as a second opinion. The diagnosis raises the accuracy up to 95%, and is based on image analyses made by leading experts. The software works as a digital diagnostic support system for the physician[1].

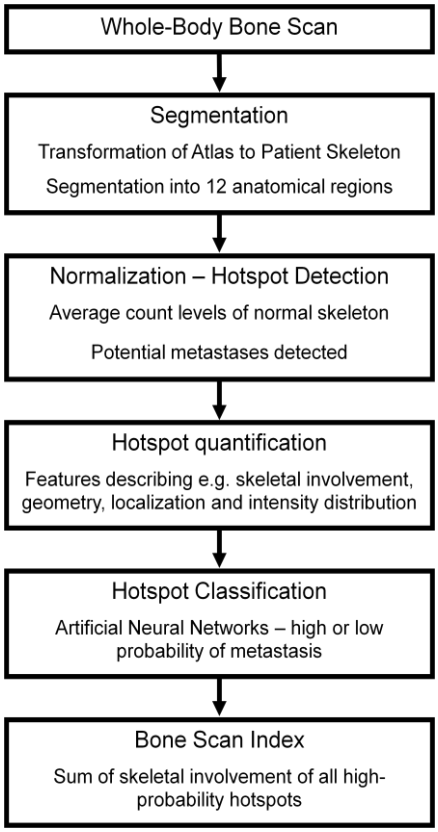

Figure 1. The above diagram illustrating the different steps of the quantification method in EXINI[1].

The validation and development of BSI has been studied, in terms of reproducibility and application for determining extent of disease and monitoring progression[5]. However, the determination of BSI does not take into account attenuation of the emitted photons, which might influence the result of BSI estimates. The effect of attenuation is illustrated in Figure 2 where the left anterior detector measures a higher count rate compare to the right posterior detector. Since the probability of metastasis detection depends highly on the signal-to-noise ratio the left detector is more probability to detector the lesion as compared to the right.

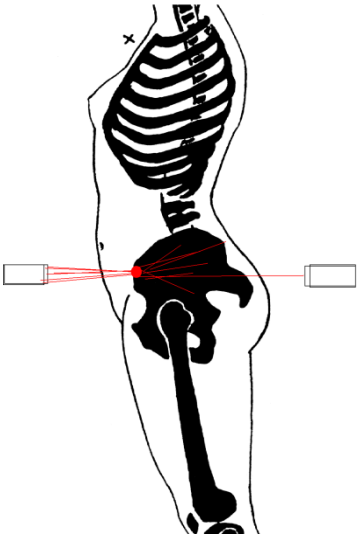

Figure 2. Description of the attenuation effect in the body.

In this study our goal was to study how the photon attenuation in the patient might influence the result of BSI. This was made in a theoretical study with a clinically realistic anthropomorphic computer phantom connected to an accurate scintillation camera simulation tool. We have defined the normal activity distribution close to a clinical MDP study and defined the virtual scintillation camera as close as possible to a clinical system. Also we have tried high activity distribution to create a "low-noise simulation".

2. Method & Materials

Accurate estimation of the 3D in vivo activity distribution is important for dose estimation in nuclear medicine, because dose distributions within human body are not directly measurable. One of the most powerful ways of estimating the dose distribution in the human body is through the use of different computational phantoms coupled with Monte Carlo transport algorithms.

a. The Monte Carlo Method

The Monte Carlo (MC) method is useful for obtaining numerical solutions to problems which are too complicated to solve analytically. It was named by S. Ulam, who in 1946 became the first mathematician to dignify this approach with a name (the name, which derives from the famous Monaco casino, emphasizes the importance of randomness, or chance, in the method), in honour of a relative having a propensity to gamble[6]. Nicolas Metropolis also made important contributions to the development of such methods. In Photon transport calculation, MC is based on stochastic mathematical simulation of the interactions between photons and matter. MC is particularly important in statistical physics, e. g. photon interaction in matter, where systems have a large number of degrees of freedom and quantities of interest cannot be computed exactly. In MC simulations photons are emitted from an isotropic point source into the solid angle specified by the focal distance and the x-ray field dimensions, and followed while they interact with the phantom according to the probability distributions of the physical processes that they may undergo: photo-electric absorption, coherent (Rayleigh) scattering or incoherent (Compton) scattering.

b. The NCAT Phantom

The Monte Carlo simulation of a scintillation camera measurement is very useful is a realistic patient-like computer phantom can be used. There have been several phantom developed and published and one of the most accurate and flexible is the NCAT software/phantom[7], see developed by Dr Paul Segars presently at the Duke University. This software creates 3D voxel matrices representing the distribution for both the attenuating media and the activity distribution of a patient. These organs are based on non-uniform rational basis spline (NURBS), which is a mathematical model used in computer graphics for generating and representing curves and surfaces. NURBS provide the flexibility to design a large variety of shapes by manipulating control points, which makes it possible to easily modify organ volumes and body contours. The main organs in the NCAT phantom is based on segmented body contour and internal organs from the Visible Male CT images set and NURBS-based smooth organ models have been generated from these images. The software is controlled by an input file were dimension and voxel resolution can be defined in addition to anatomical data such as dimensions of the phantom. The resulting NCAT voxel images provides both realistic anatomical structures and the flexibility to describe anatomical variations among patients[8].

c. The Monte Carlo program SIMIND

The Monte Carlo simulation code, SIMIND, is mainly design to simulate clinical scintillation cameras and SPECT systems and can easily be modified for almost any type of calculation or measurement encountered in SPECT imaging. The SIMIND system consists of two main programs, then CHANGE program and the SIMIND simulation program. The CHANGE program provides a menu-driven way of defining necessary parameters for the system that will be simulated. The system values that are set here will be saved as input files for SIMIND which then is the program that actual makes the Monte Carlo simulation. The result from the SIMIND is then written to various results files including energy spectrum and projection images. The common way of running SIMIND is by using command files. This is very convenient since each simulation usually takes considerably time. SIMIND contains several simulation flags which the user easily can turn on and off. These flags represents different features such as SPECT simulation, simulation of photon interaction in the phantom, the addition of a collimator and a backscattering compartment behind the crystal and so on[9].

d. Tumor Locations in NCAT patients

The NCAT software provides an accurate model of a normal skeleton. However, there is no feature in NCAT to create tumors in the skeleton. Therefore a special program, further in the text denoted as the IDL-VM, was used to arbitrary define tumors. The program has a Graphical User Interface (GUI-interface) where the user point to a location by a hair-cross using three different views (transversal, coronal and sagittal) as can be seen in Figure 3. The user then specifies the radius of the ellipsoid in three dimensions and pixel units together with a value corresponding to the number of photons emitted per voxel. The program then replaces the voxel values created by the NCAT software with the new voxel value given by the user. This can be repeated many times. The final results are then stored as voxel matrices. An alternative has been used in this work when the tumor location, dimension and activity value are stored in an input file that the SIMIND program can read. Each line

in such an input file defines one tumor. The replacement of the voxel values in then made in SIMIND rather than in the IDL-VM program.

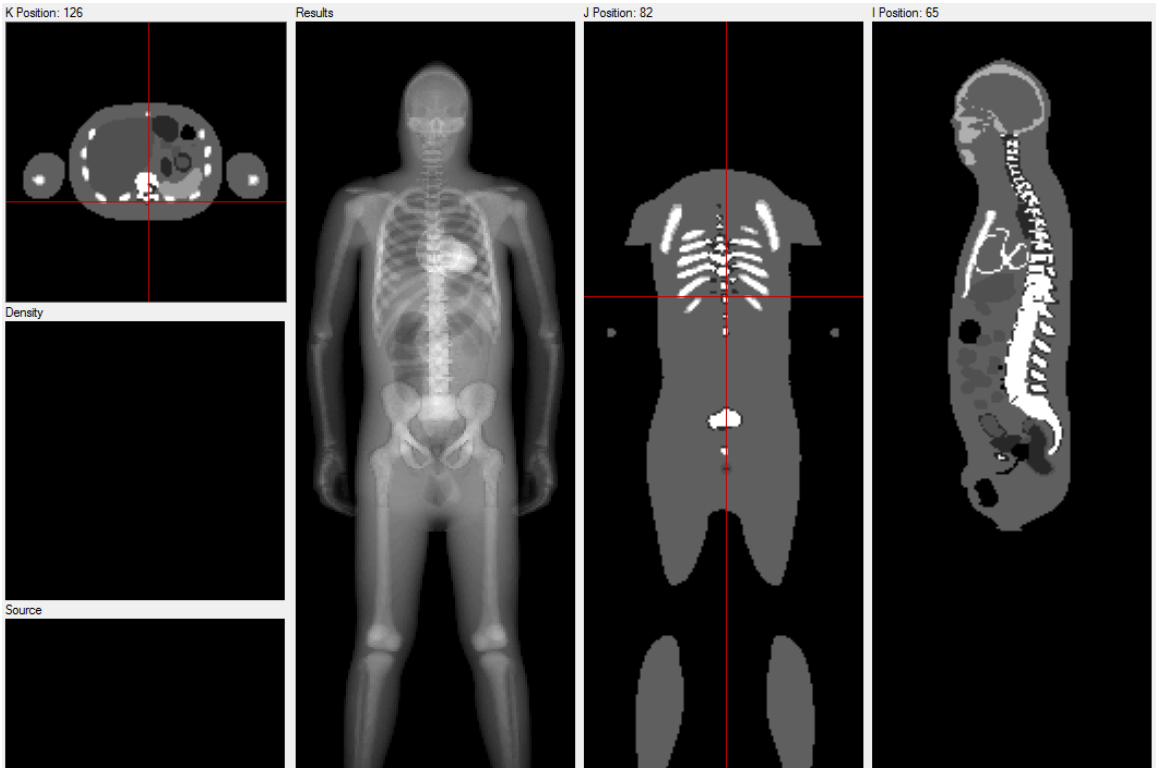

Figure 3. 3D - NCAT, whole body male phantom in IDL-VM. I, J and K directions (cf. figure 3) are seen at the top of the figure and the values in front of the directions are pixel positions.

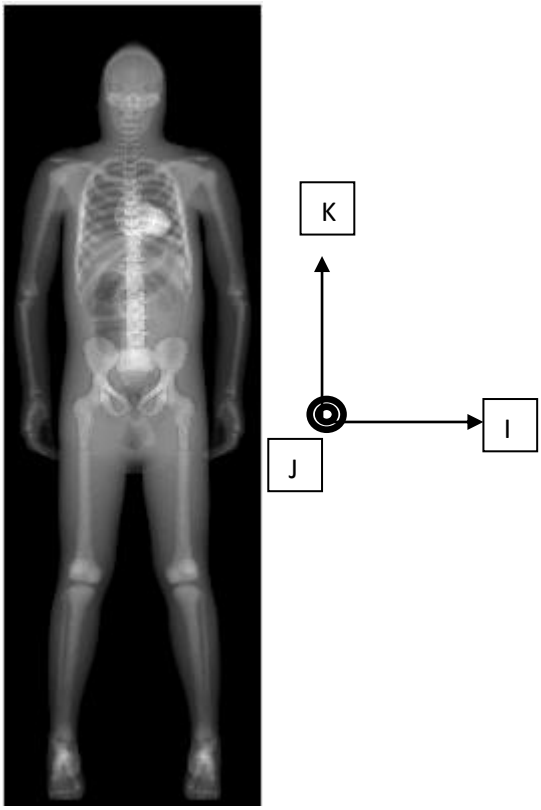

Figure 4. The I-, J- and K-direction for the NCAT phantom that is further used when defining the tumor location. The image shows the normal activity distribution.

e. The Procedure for Tumor Definitions

Several tumors were positioned at different locations in the skeleton of the phantom (Fig 5-7) and then stored in input files. To decide relevant locations for positioning the tumors in the phantom skeleton bone scan images from different real patients were studied in EXINI. The most interesting tumors locations were those that could not be seen either from the anterior or posterior side or those areas with most tumors. For example, tumors in pelvis, spine, shoulder and ribs where considered to be most relevant in our study (Fig. 8-9). The procedure for tumor definition is as follows.

The NCAT-male whole body phantom was loaded into IDL-VM. The tumors were positioned at different places as described above (Fig. 5-7). At these positions the tumors were moved in the J-direction (Fig. 3-4). The tumors were in this way moving towards or ahead the anterior or posterior camera. For the sake of simplicity, the shape for the tumors was kept ellipsoidal, for example, 2x2x2 or 1x1x1 pixels. The intensity in the IDL-VM was set to 200; the pixel value that defines the amount of counts that distributes between the whole body and the tumor. The absolute activity was defined after the SIMIND simulation; notify that the intensity here does not affect the total counts. New tumor position was obtained by moving the tumor one pixel length in the j-direction. For every new position one output file was simulated. An input (the tumor) was saved into an external file which could later on be invoked from SIMIND.

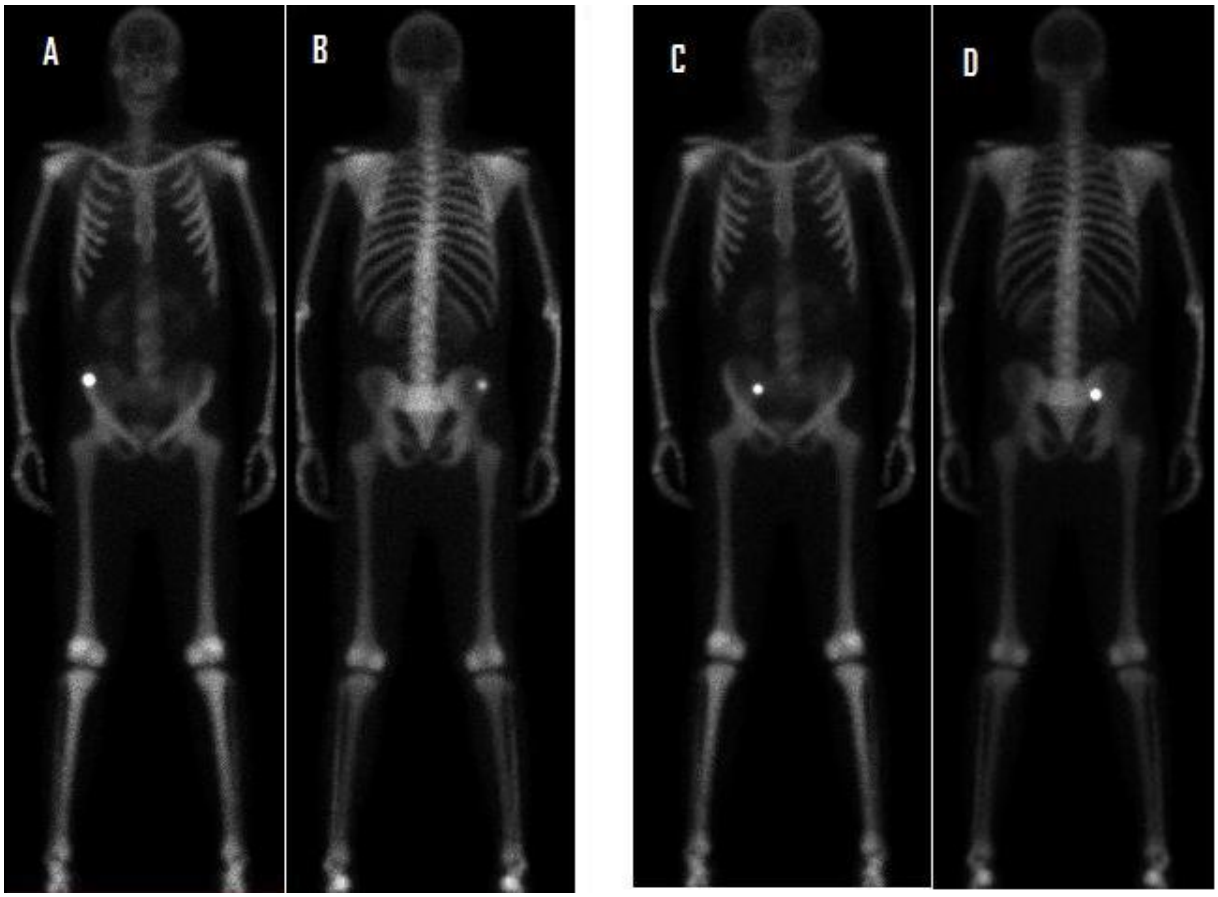

Figure 5. Tumor positioned in the pelvis, (2 x 2 x 2) pixels; the anterior image (A) and posterior image (B); another tumor in exactly same position but with different size, (2 x 2 x 2) pixels was placed; the anterior image (C) and posterior image (D).

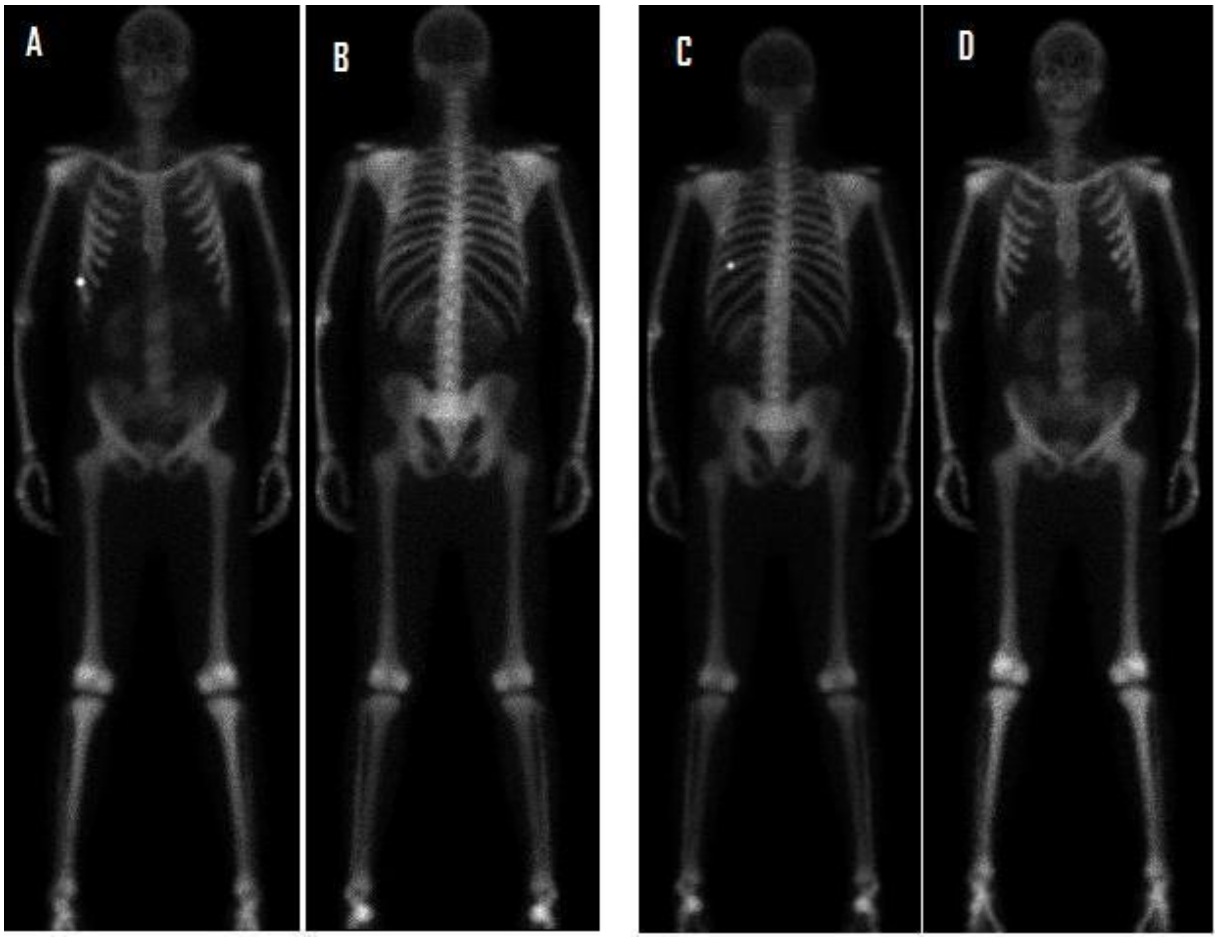

Figure 6. Tumor position in anterior rib, (1 x 1x 1) pixels; the anterior image (A) and posterior image (B). Tumor positioned in a posterior rib, (1 x 1x 1) pixels; the anterior image (C) and posterior image (D).

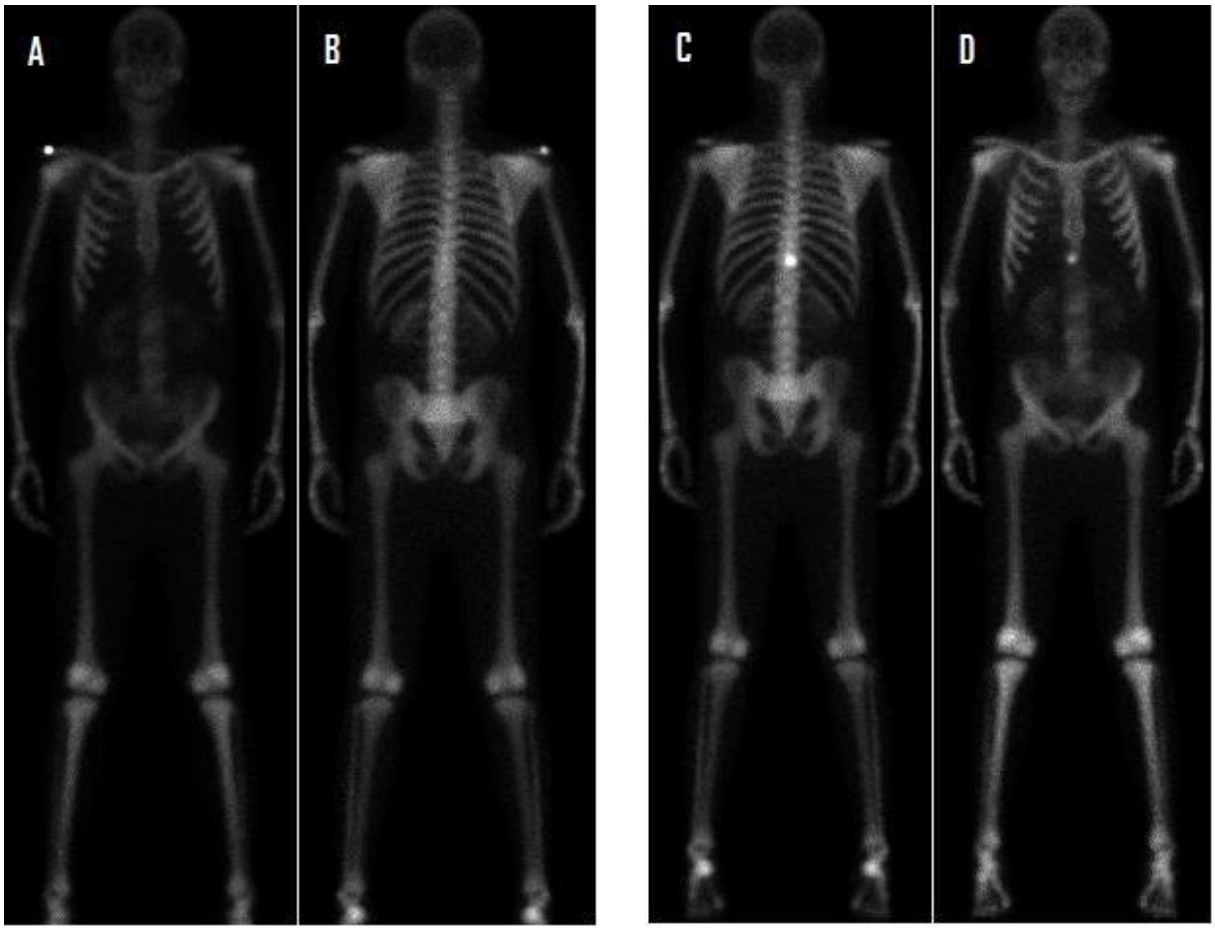

Figure 7. Two tumors were positioned in the shoulder; (2 x 2 x 2) pixels, (showed above) and (1 x 1 x 1) pixels (not shown here); the anterior image (A) and posterior image (B). Also a tumor was placed in the Spine, (2 x 2 x 2) pixels; the anterior image (C) and Posterior image (D).

How these tumors were located and then simulated will be described in detail in the following steps.

f. Scintillation Camera Monte Carlo Simulations

Our approach is to compare anterior and posterior counts for different tumor localizations in the skeleton. This part of the work is based on Monte Carlo simulation with SIMIND and the NCAT phantom. The most problematic areas in terms of tumor visibility in the skeleton were identified in clinical images with EXINI.

The scintillations camera that was simulated was a General Electric (GE) Millennium VG with LEHR collimator with round parallel holes. Cover and crystal material were aluminum and NaI(Tl) respectively. A 20% energy window was used. For complete gamma camera characteristic, see Appendix 3.

The input file (the tumor) was invoked with a simple command to create image. Two different switches have been used, /FZ and /IF. FZ-switch calls the Zubal file where the NCAT-phantom is defined. /IF - switch calls to the isotope routine for the emission photons where the default routine is a spectra routine that read information about energy and abundance from a text file. The output file is beside the .res file a file called name.a00 which contains 64 float 2x2 projections. Also is stored the .h00 file which is an interfile header file. This file may be of interest to use for display purposes, but it had to be converted into an integer file, which will be described in the next paragraph.

g. Scaling of Simulated SIMIND Images

The SIMIND program provides images that is normalised to represent a measurement of an activity distribution of 1 MBq and an acquisition time of 1 sec. This is true even if the simulation has been made with a very high number of photon histories. The images are also stored as floating point values. These images can therefore not directly be converted to integers which is the common format for display on a clinical medical imaging processing system. The images need therefore to be scaled to proper count levels. Furthermore, the noise distribution is somewhat ambiguous since SIMIND use several types of variance reduction methods to increase the calculation speed. The common way of obtaining realistic scintillation camera images is therefore to make a very low-noise SIMIND simulation and after scale to proper count level and add Poisson distributed noise. This has been done in the present work using an IDL program. The scaling where based on an administered activity of X MBq and an acquisition time corresponding to X cm/min for a 2m patient. After scaling Poission distributed noise where added using an IDL routine (POIDEV). Finally, integer Interfile files was created with appropriate header files.

Also the activity in Becquerel, camera velocity noise and whole body simulation must be defined. The camera velocity was set to a minimum, 1cm per minute and the activity was set to 1500MBq.

h. Analysis and Data Processing

We used a freeware program (X)MedCon to convert Interfile files from scaled SIMIND images to DICOM file format readable by the clinical workstation Xeleris. (X)MedCon is an open source toolkit for medical image conversion. It´s possible in (X)MedCon to exchange medical images between different processing tools very easily, which otherwise remains for many researchers a time consuming side-issue.

The DICOM files were then imported into the Xeleris computer where a line-profile was drawn for every image (anterior and posterior), see figure 10. Using the line spectrum, one could see the maximum and minimum intensity. The average count around the maximum was calculated for both anterior and posterior image. The rest of the spectrum was considered as background which was subtracted, see figure 11. The net counts were then calculated and plotted both for anterior and posterior images.

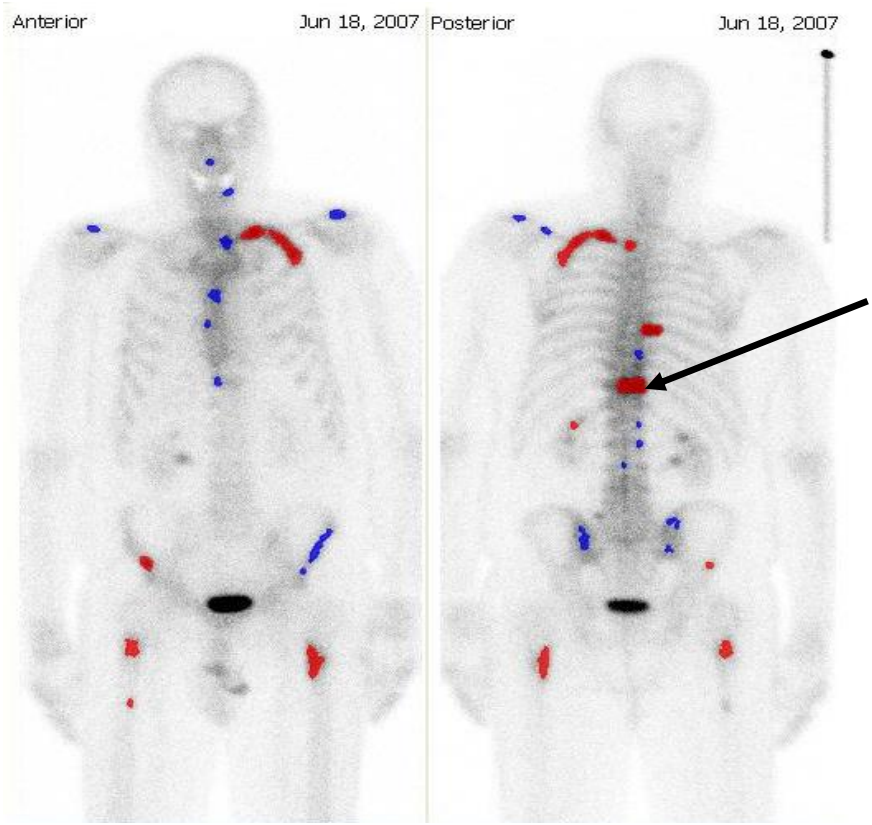

Figure 8. Two clinical bone scan images evaluated in EXINI, where e.g. a possible tumor can be observed in the spine in the posterior image. The red spots (hotspots) have higher probability to be metastases than the blue spots.

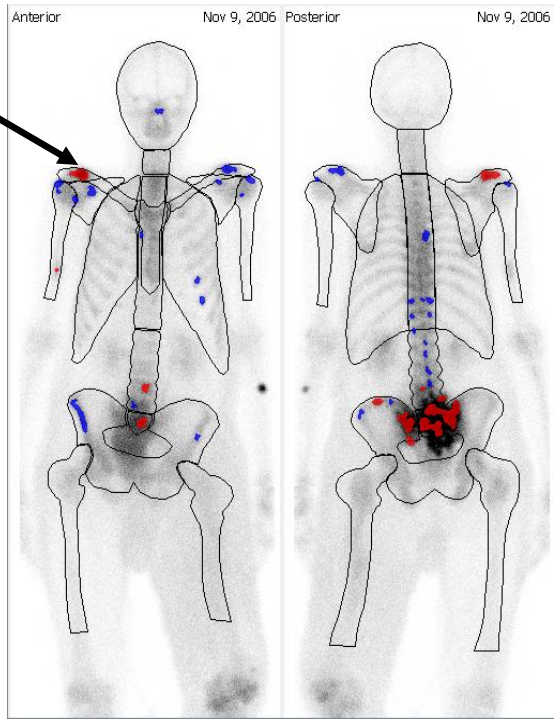

Figure 9. Another example of a possible tumor, but this time in another patients shoulder.

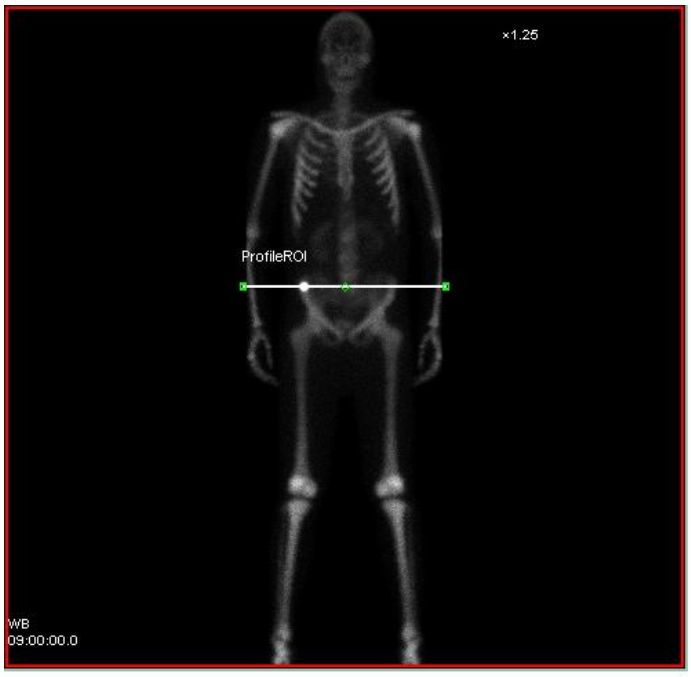

Figure 10. An example of an anterior image with a (2 x 2 x 2) pixels tumor in the pelvis and a line profile has been placed through the tumor.

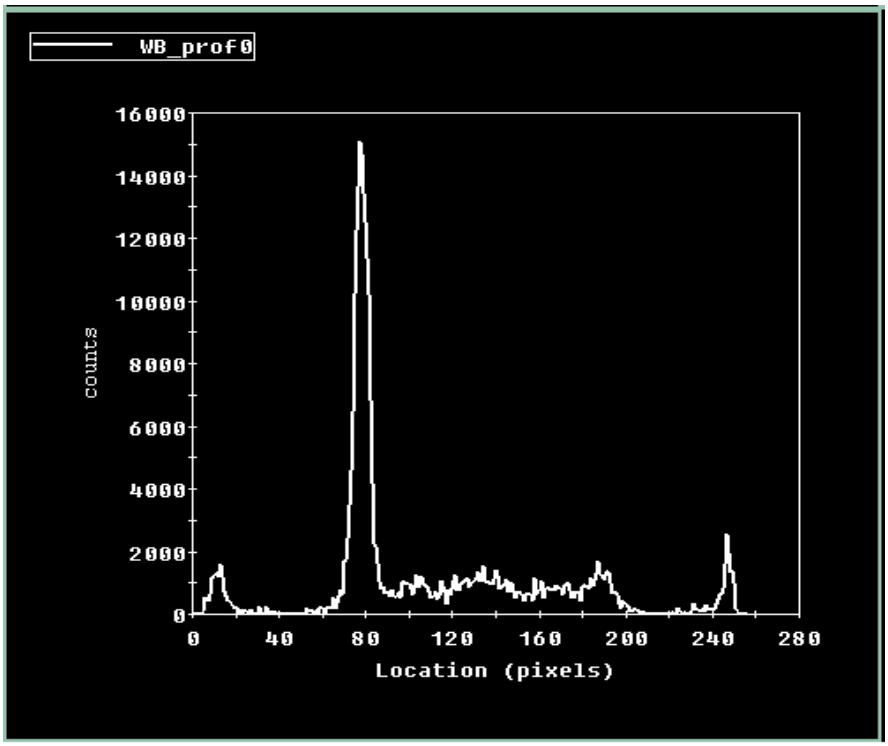

Figure 11. The Line spectrum for the (2 x 2 x 2) pixels tumor in Pelvis is shown here; the pick, maximum intensity is in pixel location 80. The background count (location 69-0 and 91-256) was subtracted from location 70-90 where the pick is.

3. Results

The results for the tumors with different sizes and in different places are shown in figure 12-18. The figures are showing how the net counts per 240 seconds (Y-axis) are changing with distance (X-axis) in the J-direction.

The counts increase when the tumor is approaching the camera anterior or posterior, and the counts decreases when the tumor is moving away from the anterior and posterior cameras.

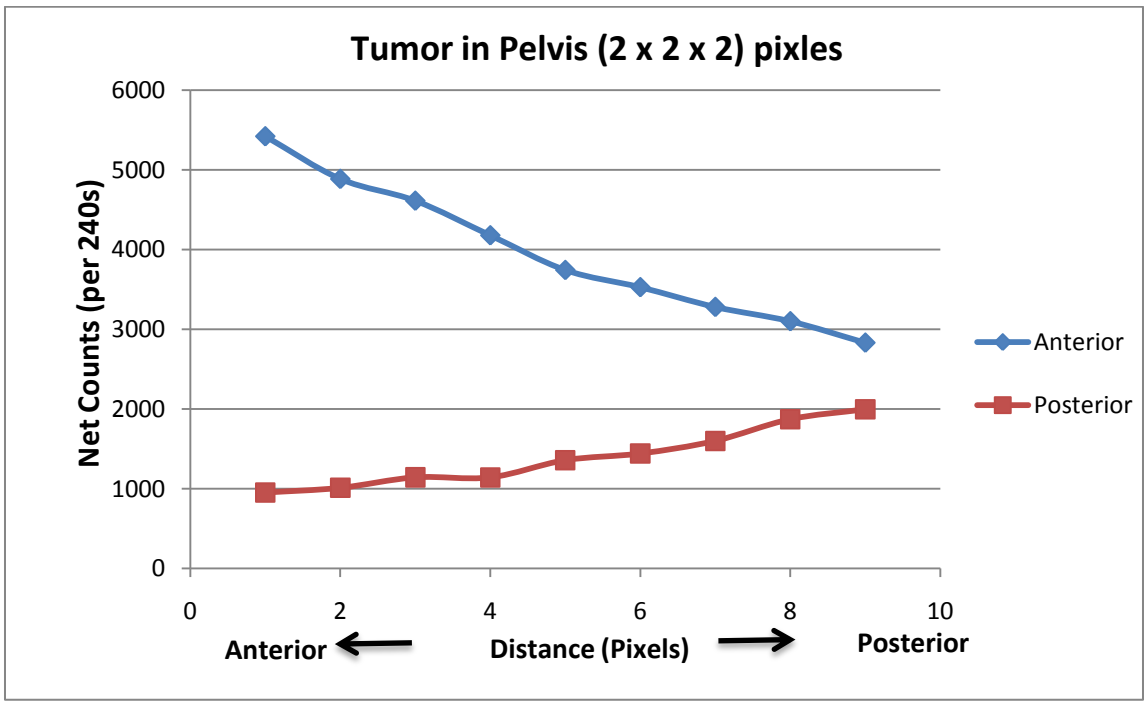

Figure 12. The counts for posterior and anterior for a (2 x 2 x 2) pixels tumor in the Pelvis at different J-directions (distance in pixels) (cf. Fig. 5-A,B). The counts are collected in 240 seconds scanning. The anterior counts are much higher than the posterior counts. The lowest count for the anterior is a bit below 3000 and the highest count for the posterior is little bit above 2000.

The posterior counts increases smoothly in the entire distance. The Anterior counts fall rapidly all the way. It moves between 5500 and 2800 as the tumor approaching to posterior camera.

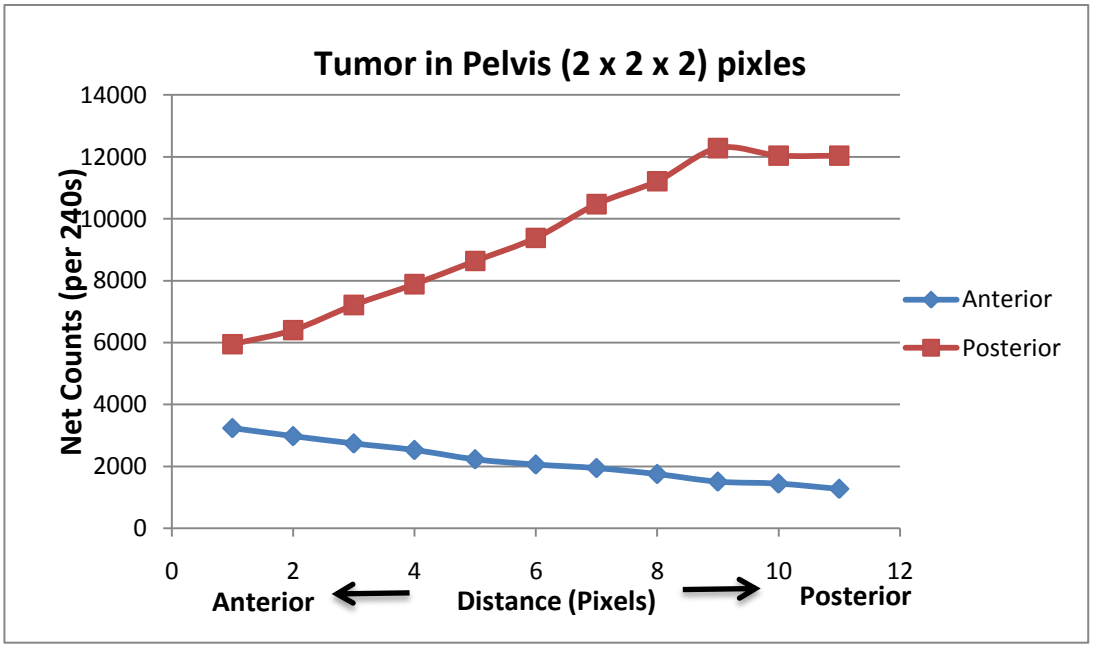

Figure 13. The counts from posterior and anterior images for a (2 x 2 x 2) pixels tumor in the spine at different J-directions (distance in pixels) (cf. Fig 5-C,D). The counts are collected in 240 seconds scanning. The posterior counts are much higher than anterior counts. The lowest count for posterior is below 6000 and the highest count for anterior is little bit above 3000.

The posterior counts increases rapidly, from almost 6000 to 12000 as the tumor moves further in the spine and approaching the posterior camera. The anterior counts do not falls rapidly, it moves between 3000 and 1200 as the tumor approaching to camera, posterior.

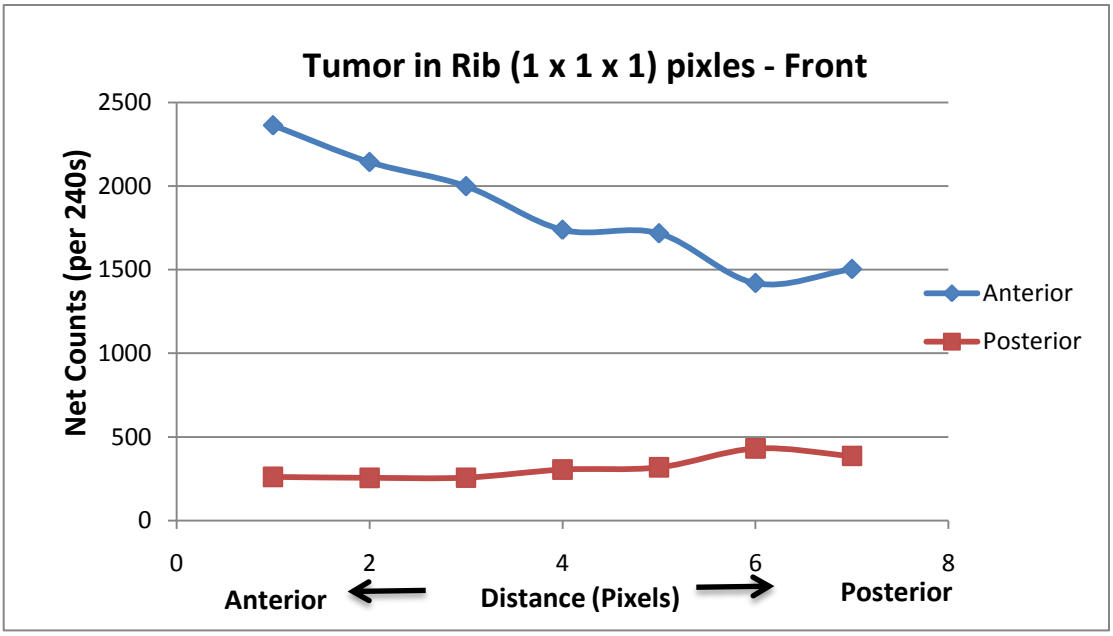

Figure 14. The counts for posterior and anterior for a (1 x 1 x 1) pixels tumor in the Rib in front of the body, at different J-directions (distance in pixels) (cf. Fig 6,A-B). The counts are collected in 240 seconds scanning. The anterior counts are much higher than posterior. The lowest count for the anterior is 1500 and the highest count for the posterior is little bit below 500.

The anterior counts fall of rapidly, from almost 2300 to 1500 as the tumor moves further in the Rib and approaching the posterior camera. For the Posterior counts seems a very weak increase as the distance increases and the tumor approaching the posterior camera. The counts increase from 260 to 380.

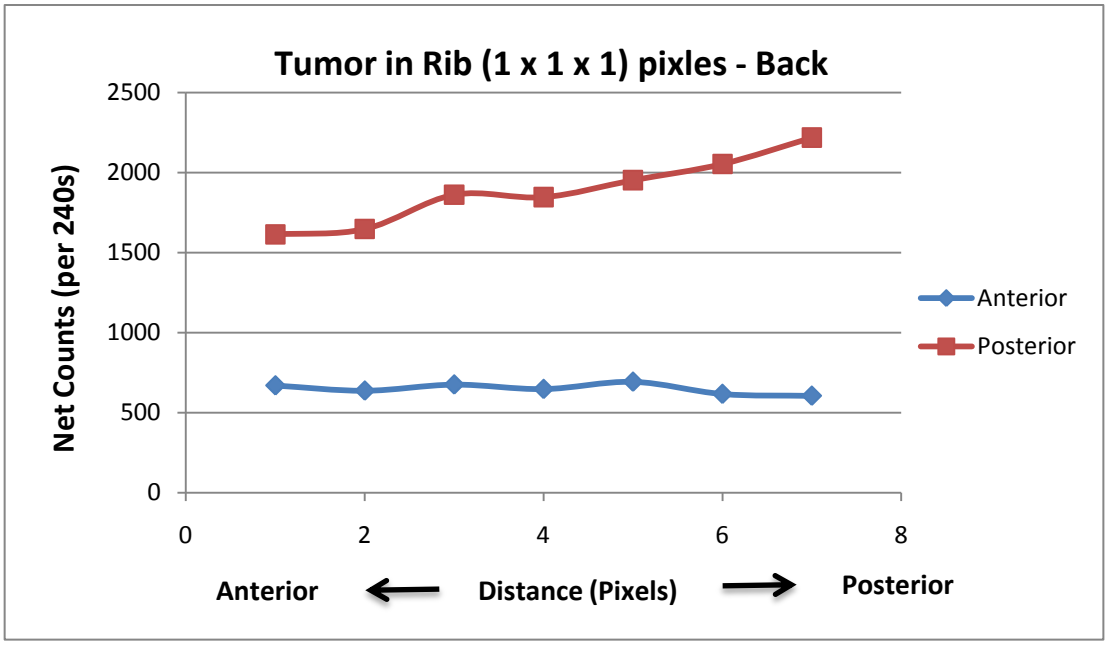

Figure 15. The counts for posterior and anterior for a (1 x 1 x 1) pixels tumor in Rib on the backside of the body, at different J-directions (distance in pixels) (cf. Fig. 6-C,D). The counts are collected in 240 seconds scanning. The highest count for the anterior is above 600 and the lowest count for the posterior is a bit above 1600. The posterior counts increases from almost 1600 to 2200 as the tumor moves further in the Rib, and approaching posterior camera. Anterior counts decreases slightly as the tumor approaching the posterior camera. The counts are decreasing from 670 to 600.

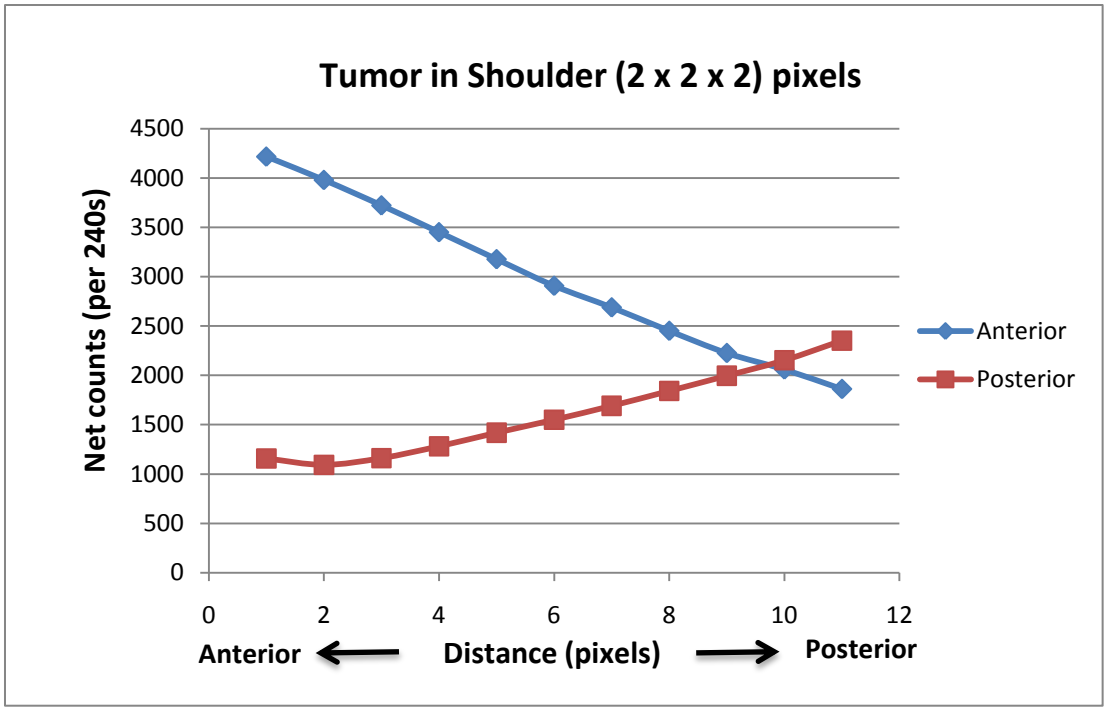

Figure 16. The counts for posterior and anterior for a (2 x 2 x 2) pixels tumor in the shoulder, at different J-directions (distance in pixels) (cf. Fig 7-A,B). The counts are collected in 240 seconds scanning. The Anterior counts are decreasing and the posterior counts are increasing when tumor is approaching the posterior camera. The curves have the same count value at distance 10. The lowest count for anterior is about 20% lower than the highest posterior count.

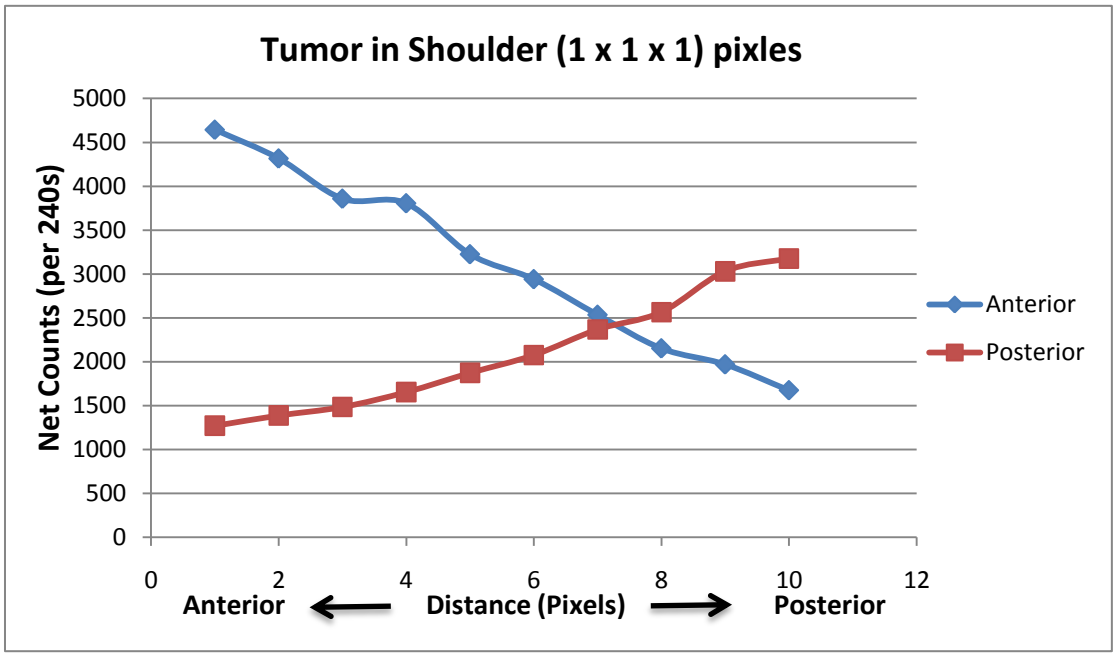

Figure 17. The counts for posterior and anterior for a (1 x 1 x 1) pixels tumor in the shoulder, at different J-directions (distance in pixels). The counts are collected in 240 seconds scanning. The trend is look the same as the figure 18 , the (2 x 2 x 2) pixels tumor. But the only difference is that the curves are crossing at distance 7.

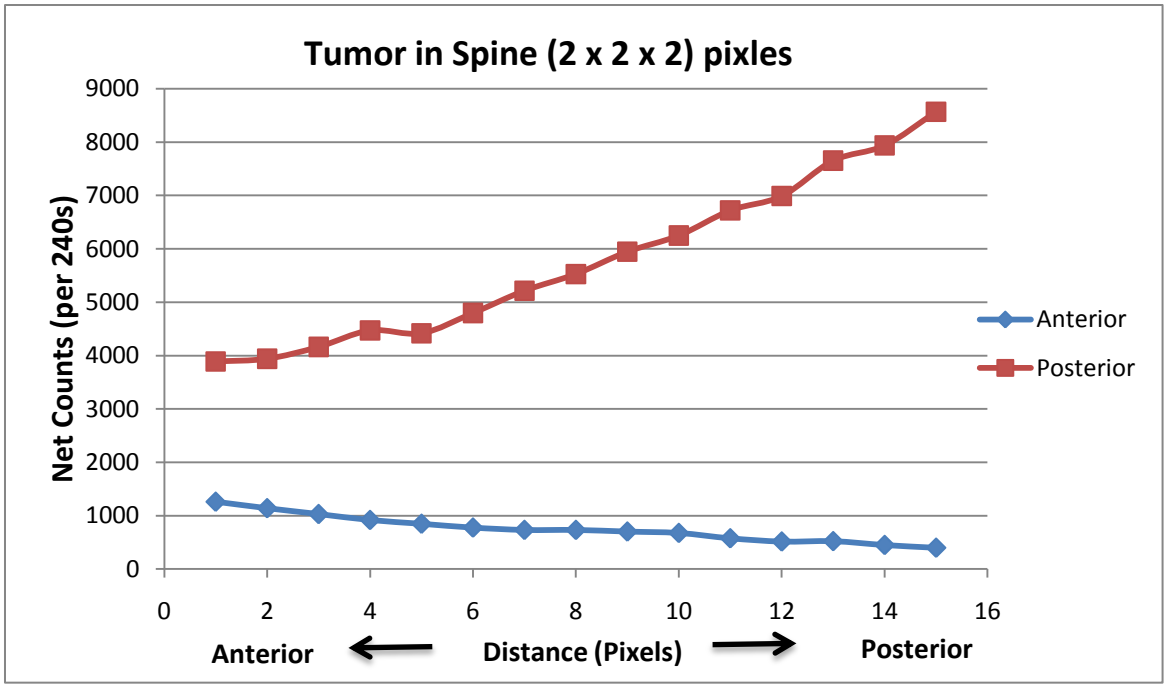

Figure 18. The counts for posterior and anterior for a (2 x 2 x 2) pixels tumor in the spine, at different J-directions (distance in pixels) (cf. Fig 7-C,D). The counts are collected in 240 seconds scanning. The posterior counts increases from 3900 to 8600 and the anterior counts falls off smoothly from 1250 to 400 as the tumor moving towards the posterior camera. the difference between the highest and lowest for the anterior and posterior counts is about 2600.

4. Discussion

To make the phantom (3D - NURBS-based cardiac-torso NCAT, whole body male phantom) images similar as clinical bone scintigraphy images, according to Procedures Guidelines For Tumor Imaging[10], total counts was set to 1.5 million. Several activities and velocities were tested to get to the 1.5 million counts. But because of the week statistic, the amount of activity that has been specified in the guidelines was ignored; the activity was increased to almost 10 times higher. This generated less variation in the data points and comparison could be performed between the mean anterior and posterior net counts and the influences of attenuation effect were visualized.

The resolutions and visibilities of structures in the body with nuclear medicine perhaps are less than most other imaging techniques, such as CT or MRI. It´s due to the inherent construction of the gamma camera as well as poor counting statistic; due to the small amount of radiopharmaceuticals or radiotracers used, furthermore, the attenuation of radiation will also influence the visibility. The attenuation effect can't easily be measured exactly. When it comes to bone metastases in the skeleton, the same factors should be considered here. This study has shown that the most problematic areas when it comes to visibility for bone metastases is those areas where either the bone is very thick or more soft tissues like other organs are surrounding the bone. For example, tumor in the spine and pelvis shows that the differences between anterior and posterior counts are quite high. Because the activities that have been used in these simulations are very high, so the small amount of radiopharmaceutical´s on visibility is minimal, and the only thing that could matter, should be the differences in distance in the body, and attenuation is directly connected to the distance. So attenuation correction should be considered when bone scintigraphy images are being studied or BSI is being calculated. Another problematic area that should also be considered is the Rib both in front and back of the body, even though the rib bone is not as thick as the spine or the pelvis. It´s also probably because the distance is fairly large here so the photons are passing many organs and other bones before they detects in the gamma camera.

Software restrictions have made so that it have not been able to test different forms of tumors, (not just ellipsoidal tumors). It would be interesting to further examine the form of the tumors in EXINI and then try to recreate the tumor shape in the phantom. Also because of the software limitations it was not possible to place tumors correctly in smaller bones that had curved form, so occasionally part of the tumor would land up in the soft tissue, which might had effects on the net counts.

5. Conclusion

Attenuation effects in the BSI are significantly large and had to be taken into account. The result in this study shows that as the tumor approaching each camera, either it´s anterior or posterior, the amount of net counts increases or decreases considerably. Most problematic areas in terms of tumor visibility are those areas where the amount of soft tissue is high or where the bone is very thick. By watching the trend of the curves these problematic areas can be identified.

6. Acknowledgements

Probably this last section is more important than the entire work. This work wouldn´t have be done without these people that i would like to mention.

First of all I would like to thank my supervisors *Peter Bernhardt* at the Department of Radiation Physics, at Gothenburg University, Sweden who have taken the time and trouble to alert me about errors and solving problems on the way, and Michael Ljungberg,
Medical Radiation Physics, Department of Clinical Sciences, Lund University, Sweden, for his fast response for all the questions that I asked.

I would like to specially thank *Esmaeil Mehrara*, PhD Graduate at the Department of Radiation Physics, at Gothenburg University, Sweden for all his good advises and our good discussions through the project.

Thanks to *Lars Edenbrandt*, Professor in Clinical Physiology and Nuclear Medicine at Gothenburg University, Thanks to *Lena Johansson*, BMA, for helping me with EXINI during the project and giving me helpful comments after reading my report, Thanks to *Tobias Lundblad*, sjukhusfysiker, for all his help to make the softwares work.

Thanks to Nuclear medical department at *Sahlgrenska university hospital* for having me there and stood out with me.

Last but not least I want to thanks my wife, Nilufar and two sons, Diaco and Ario for supporting me in all laughter and tears, not only during this project but throughout at least last 5 years.

7. References

1. R. Kaboteh MS, M. Suurkula, M. Lomsky, P. Gjertsson, J. Richter, K. Sjöstrand, M. Ohlsson and L. Edenbrandt Automated Quantitative Bone Scan Analysis. 2009.
2. Sven Almér GG, Sven-Ola Hietala, Bengt Erik Johansson, Lennart Johansson. *Nuclear medicine*, 1998.
3. I.C.R.P. Report of the Task Group on Reference Man. [ICRP Publication] No. 23. 1975.
4. Edenbrandt L. EXINI.
5. Imbriaco M, Larson SM, Yeung HW, Mawlawi OR, Erdi Y, Venkatraman ES, et al. A new parameter for measuring metastatic bone involvement by prostate cancer: the Bone Scan Index. *Clin Cancer Res* 1998;4(7):1765-72.
6. Hoffman P. The Man Who Loved Only Numbers: The Story of Paul Erdos and the Search for Mathematical Truth. 1987.
7. Segars WP. Development and application of the new dynamic NURBS-based cardiac-torso (NCAT) phantom, in Biomedical Engineering. 2001.
8. Lee C, Lodwick D, Bolch WE. NURBS-based 3-D anthropomorphic computational phantoms for radiation dosimetry applications. *Radiat Prot Dosimetry* 2007;127(1-4):227-32.
9. Ljungberg M. Monte Carlo Calculations in Nuclear Medicine: Applications in Diagnostic Imaging. 1998:308.
10. Emilio Bombardieri CA, Richard P. Baum, Angelica Bishof-Delaloye,, John Buscombe JFC, Lorenzo Maffioli, Roy Moncayo, Luc, Mortelmans SNR. BONE SCINTIGRAPHY PROCEDURES GUIDELINES FOR TUMOUR IMAGING. 2003.

Appendix 1

```
=====Code Section 4 NCAT   ===========
hrt_myoLV_act               1  1060   1
hrt_myoRV_act               2  1060   1
hrt_myoLA_act               3  1060   1
hrt_myoRA_act               4  1060   1
hrt_bldplLV_act             5  1060   1
hrt_bldplRV_act             6  1060   1
hrt_bldplLA_act             7  1060   1
hrt_bldplRA_act             8  1060   5
body                        9  1000   1
liver                      10  1060   1
gall_bladder               11  1026   1
lung                       12   260   1
st_wall                    13  1030   1
st_cnts                    14  1060   1
kidney                     15  1050   10
spleen                     16  1060   1
rib                        17  1410   15
spine_head_activity        18  1330   50
spine_process_activity     19  1330   50
pelvis_activity            20  1290   50
bone_cartilage             21  1100   100
artary                     22  1060   1
vein                       23  1060   1
bladder                    24  1040   80
prostate                   25  1045   1
ascend_large_intest        26  1030   1
transc_large_intest        27  1030   1
desc_large_intest          28  1030   1
small intestine            29  1030   1
rectum                     30  1030   1
sem_vess                   31  1030   1
vas_def                    32  1030   1
testicular                 33  1040   1
ascend large_int           34    10   1
transve large_intest       35    10   1
descend large_intest       36    10   1
small intestine air        37    10   0
rectum air                 38    10   0
ureter                     39  1030   0
urethra                    40  1030   0
lymph normal               41  1030   0
lymph abnormal             42  1030   0
airway tree activity       43  1030   0
uterus_activity            44  1030   0
vagina_activity            45  1030   1
right_ovary_activity       46  1030   1
left_ovary_activity        47  1030   1
fallopian tubes_activity   48  1030   1
free                       49  1000   0
free                       50  1000   0
```

Appendix 2

```
=====Code Section 4 NCAT   ========
hrt_myoLV_act              1  1040   1
hrt_myoRV_act              2  1040   1
hrt_myoLA_act              3  1040   1
hrt_myoRA_act              4  1040   1
hrt_bldplLV_act            5  1000   1
hrt_bldplRV_act            6  1000   1
hrt_bldplLA_act            7  1000   1
hrt_bldplRA_act            8  1000   1
body                       9  1040   1
liver                     10  1060   1
gall_bladder              11  1026   1
lung                      12   394   1
st_wall                   13  1030   1
st_cnts                   14  1000   1
kidney                    15  1050   15
spleen                    16  1060   1
rib                       17  1400   23
spine head                18  1400   23
spine process             19  1400   23
pelvis                    20  1400   23
bone_cartilage            21  1400   23
artery                    22  1000   1
vein                      23  1000   1
bladder                   24  1000   8
prostate                  25  1045   1
ascend_large_intest       26  1030   1
transc_large_intest       27  1030   1
desc_large_intest         28  1030   1
small intestine           29  1030   1
rectum                    30  1030   1
sem_vess                  31  1000   1
vas_def                   32  1000   1
testicular                33  1000   1
ascending large intest    34  1000   1
transverse large intest   35  1000   1
descending large intest   36  1000   1
small intestine           37  1000   1
rectum                    38  1000   1
ureter activity           39  1000   1
urethra activity          40  1000   1
lymph normal activity     41  1000   1
lymph abnormal activity   42  1000   1
airway tree activity      43  1000   1
uterus_activity           44  1000   1
vagina_activity           45  1000   1
right_ovary_activity      46  1000   1
left_ovary_activity       47  1000   1
fallopian tubes_activity  48  1000   1
```

Appendix 3

Gamma camera	GE Millennium VG
Collimator	LEHR, with parallel round holes
Phantom soft tissue	H2O
Phantom bone tissue	Bone
Cover material	Aluminium
Crystal material	NaI
Backscatter material	Lucite
Scintillation Camera Parameters	
Photon energy	140 keV
Crystal: Half Length/Radius	104 cm
Crystal: Thickness	1.587 cm
Crystal: Half Width	27 cm
Height to Detector Surface	25 cm
Thickness of Cover	0.1 cm
Phantom type	Code based NCAT Phantom (4 byte float)
Source Type	Code based NCAT Phantom (4 byte float)
Energy Window	20%
Energy Resolution (140 keV)	9.8%
Intrinsic Resolution (140 keV)	0.450 cm
Number of photon histories	10^9
keV/Channel	1keV
Pixel Size in simulated image	0.221cm
No of projections	2
Non Homogeneous phantom And	**SPECT parameters**
Pixel Size in Density Maps	0.5 cm
Number of CT-images	400
Collimator Parameters	
Hole Size X	0.150 cm
Hole Size Y	0.168 cm
Distance between two holes: X-direction	0.02 cm
Distance between two holes: Y-direction	0.118 cm
Displacement center hole: X-direction	0.085 cm
Displacement center hole: Y-direction	0.143 cm
Collimator Thickness	3.5 cm
Shape	Hexagonal
Type of Collimator	Parallel
Image Parameters and other settings	
Matrix size image I	256
Matrix size image J	1024
Matrix size density map I	128
Matrix size source map	128
Energy spectra channels	512
Matrix size density map J	128
Matrix size source map J	128